ARTICLE

Three-Step Change in Uniaxial Negative Thermal Expansion by Switching Supramolecular Motion Modes in Ferromagnetically-Coupled Nickel Dithiolate Lattice†

Received 00th January 20xx,
Accepted 00th January 20xx

DOI: 10.1039/x0xx00000x

Masato Haneda,[a] Kiyonori Takahashi,[a,b*] Naohiro Hasuo,[a] Rui-Kang Huang,[a,b] Chen Xue,[a,b] Jia-bing Wu,[a,b] Shin-ichiro Noro,[a,c] and Takayoshi Nakamura[a,b,d*]

The wheel-axle-type supramolecule, (($^+$H$_3$N-C$_2$H$_4$)$_2$O)([18]crown-6)$_2$, was introduced into the crystal as a counter cation of [Ni(dmit)$_2$]$^-$. Within the crystal, [Ni(dmit)$_2$]$^-$ was arranged in a honeycomb-like structure and one-dimensional chains formed by (($^+$H$_3$N-C$_2$H$_4$)$_2$O)([18]crown-6)$_2$ penetrated each honeycomb lattice. In the supramolecular structure, ($^+$H$_3$N-C$_2$H$_4$)$_2$O behaved as a rigid axle. Two [18]crown-6 molecules, **CE1** and **CE2**, behaving like wheels, were crystallographically independent of each other, with **CE2** showing disorder. The crystal exhibited uniaxial negative thermal expansion (NTE). With increasing temperature, the disorder state of **CE2** changed, resulting in a change in the coefficient of linear thermal expansion (CLTE) of the crystal in all directions. In the $\boldsymbol{X_1}$ direction, where NTE was observed, the CLTE was relatively small at −18×10^{-6} K^{-1} in Phase I (113-133 K) in which **CE2** was static. In Phase II (143-193 K), when **CE2** starts to rotate, the CLTE of the NTE increases significantly to −74×10^{-6} K^{-1}. Furthermore, in Phase III (213-293 K), where [18]crown-6 out-of-plane motion is also involved, the NTE is extremely large with a value of −105×10^{-6} K^{-1}. Ferromagnetic interactions between [Ni(dmit)$_2$]$^-$ molecules were observed, with the Weiss temperature of +1.41 K. Multi-step changes in the mode of motion in supramolecular structures may offer new possibilities for multi-step control of the thermal expansion of crystals.

Introduction

Materials generally exhibit positive thermal expansion (PTE) because the amplitude of the anharmonic vibrations of their constituent molecules, atoms and ions increases with increasing temperature. The coefficient of linear thermal expansion (CLTE) of organic materials can be 10 times higher than that of inorganic materials.[1,2] In devices where both inorganic and organic materials are essential, such as organic light-emitting diodes,[3] organic field-effect transistors[4] and fibre-optic systems,[2] the difference in thermal expansion between the materials can cause significant damage to the device.[5] Controlling the thermal expansion of materials is therefore important to ensure stable device operation. The use of materials exhibiting negative thermal expansion (NTE) is attracting attention as a method of controlling thermal expansion.[6] The combination and compositing of NTE and PTE materials enables the control of thermal expansion, including the construction of zero thermal expansion (ZTE) materials, which does not show thermal expansion with temperature change.[5]

Due to the diverse factors involved in thermal expansion, such as thermal vibrations,[7–12] molecular rearrangements[13–19] and distortion of the coordination environment[15–17], the mechanism of NTE and how they are controlled are poorly understood in molecular materials. Since an increase in entropy can be a factor in NTE, the use of molecular motion to increase entropy in molecular crystals is widely recognized as a powerful means of achieving NTE.[23–27] However, it is usually difficult to achieve molecular motion in crystals that favor close packing.

We have already reported on the effectiveness of supramolecular strategies to achieve NTE exploiting molecular motion within crystals. In (pyridazinium)$_2$(dibenzo[24]crown-8)$_3$[Ni(dmit)$_2$]$^-_2$ crystal (dmit^{2-} = 1,3-dithio-2-thione-4,5-dithiolate), dibenzo[24]crown-8 forms a one-dimensional (1D) channel structure *via* C-H•••π and π•••π interactions with neighboring dibenzo[24]crown-8, and pyridazinium cations are incorporated into this channel. The crystal contracted in the direction perpendicular to the channels, resulting in uniaxial NTE. The NTE response is about 3 times larger above 180 K, which coincides with the temperature at which rotation of pyridazinium begins. The supramolecular approach is an effective means of achieving NTE because of the wide selection possibilities in the organic cations and crown ether derivatives to be combined. Furthermore, the physical properties of the

[a] *Graduate School of Environmental Science, Hokkaido University, N10W5, Kita-ku, Sapporo, Hokkaido, 060-0810.*
E-mail: ktakahashi@es.hokudai.ac.jp, tnaka@es.hokudai.ac.jp
[b] *Research Institute for Electronic Science, Hokkaido University, N20W10, Kita-ku, Sapporo, Hokkaido, 010-0020.*
[c] *Faculty of Environmental Earth Science, Hokkaido University, N10W5, Kita-ku, Sapporo, Hokkaido, 060-0810, Japan.*
[d] *Department of Chemistry, Graduate School of Advanced Science and Engineering, Hiroshima University, Higashi-hiroshima 739-8526, Japan.*

† Electronic supplementary information (ESI) available: Experimental section, Details of crystallography and its temperature dependence, PXRD, TG-DTA, DSC, details of dication, dielectrics measurement, input and output files of PASCal calculation. CCDC 2384649–2384662. For ESI and crystallographic data in CIF or other electronic format see DOI: 10.1039/x0xx00000x

anions and supramolecular cations that constitute the crystals express a wide range of functions.[28] In fact, we found that (4-aminopyridinium)(benzo[18]crown-6)[Ni(dmit)$_2$]$^-$ exhibits not only NTE, but also unique magnetic behavior derived from [Ni(dmit)$_2$]$^-$ and relaxor ferroelectricity derived from the molecular motion of supramolecular cations.[29]

In these crystals constructed by the supramolecular strategy, the enhancement of NTE is caused by molecular rearrangements driven by molecular motion in the crystal. To efficiently link molecular motion in a crystal to NTE, we have now designed a wheel-axle-type supramolecular cation composed of [18]crown-6 and ($^+$H$_3$N-C$_2$H$_4$)$_2$O having a linear alkoxyl chain, which was introduced in [Ni(dmit)$_2$]$^-$ crystal to form (($^+$H$_3$N-C$_2$H$_4$)$_2$O)([18]crown-6)$_2$[Ni(dmit)$_2$]$^-_2$ (**1**). The dication ($^+$H$_3$N-C$_2$H$_4$)$_2$O, which acts as an axle, interacts with two molecules of [18]crown-6, which act as wheels, *via* N-H•••O hydrogen bonds in both terminal NH_3^+ groups to form supramolecular cations. In the crystal, the [18]crown-6 not only exhibited conformational flexibility but also in-plane rotation. The crystal exhibited a two-step enhancement of the NTE associated with the changes in the motional modes of [18]crown-6, and [Ni(dmit)$_2$]$^-$ exhibited ferromagnetic behavior at low temperatures.

Result and Discussion

The crystal structure of **1** at 113 K is shown in Figure 1. The crystal system is triclinic and the space group is *P*$\bar{1}$. Within the crystal, ($^+$H$_3$N-C$_2$H$_4$)$_2$O and two molecules of [18]crown-6 are crystallographically independent, denoted **Cat**, **CE1**, and **CE2**, respectively. **CE2** shows disorder at two different sites, **CE2A** and **CE2B**, each with approximately equal occupancy, as depicted in Figure 1a. The conformer with the larger occupancy over the entire temperature range is defined as **CE2A**. In addition, one [Ni(dmit)$_2$]$^-$ (**A**) and two [Ni(dmit)$_2$]$^-$ halves (**B** and **C**) are crystallographically independent (Figures 1b and c).

As expected, the two terminal NH_3^+ groups of ($^+$H$_3$N-C$_2$H$_4$)$_2$O form N-H•••O hydrogen bonds with [18]crown-6, respectively, yielding wheel-axle-type supramolecular cations (see Table S1 in ESI for detail). These supramolecular cations stack along the [1 1 1] direction to form a chain structure consisting of **CE1•••Cat•••CE2•••CE2•••Cat•••CE1** within the chain. Due to C-H•••O interactions, adjacent **CE1** molecules exhibit an interlocking pattern that resembles two gears meshing (highlighted by the red arrows in Fig 1a and described in Table S2 in ESI for detail). Similar meshing is also observed between adjacent **CE2A•••CE2A** and **CE2B•••CE2B** pairs. The [Ni(dmit)$_2$]$^-$ anions are arranged around the supramolecular chains, so that each supramolecular chain is isolated within the crystal. The long axes of [Ni(dmit)$_2$]$^-$ **A** and **B** are oriented approximately in the [1 1 1] direction, and the molecular planes of **A** and **B** are approximately parallel and perpendicular to the (0 1 −1) plane, respectively. The [Ni(dmit)$_2$]$^-$ **A** is arranged one-dimensionally along the *a*-axis direction *via* side-by-side sulfur (S)•••S contacts of less than the sum of the van der Waals radii (Table S3 in ESI). The [Ni(dmit)$_2$]$^-$ **B** whose molecular plane is nearly orthogonal to that of **A**, has S•••S contacts with

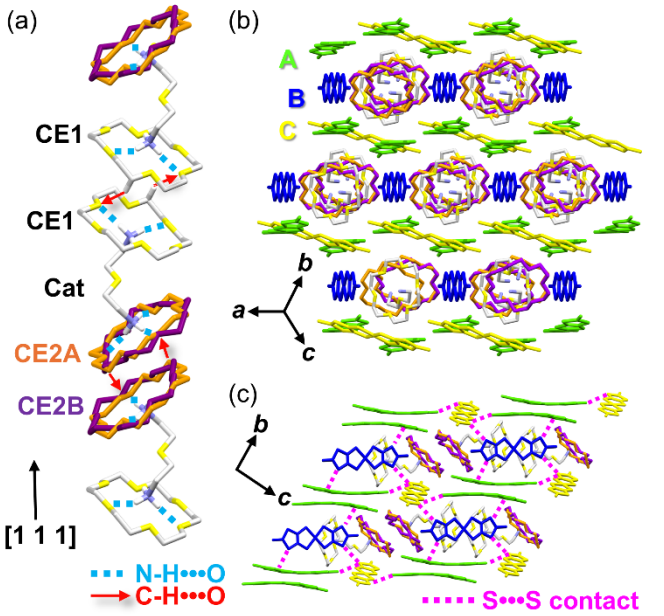

Figure 1. Crystal structure of **1** at 113 K. Hydrogen atoms are omitted for clarity except those involved in N-H•••O and C-H•••O interactions, which are described as light blue dotted lines and red arrows, respectively, in Fig.1a. The carbon, hydrogen, oxygen, and nitrogen atoms in the supramolecular cation are shown in gray, white, yellow, and light blue, respectively, except those in disordered molecules. The disorder sites of **CE2A** and **CE2B** are shown in orange and purple, respectively. The three crystallographically independent [Ni(dmit)$_2$]$^-$, which are designated **A**, **B**, and **C**, are shown in green, blue, and yellow, respectively. (a) The one-dimensional chain structure of supramolecular cations. (b) Packing structure viewed from the [1 1 1] direction. (c) Packing structure viewed along the *a* axis. Pink dotted line corresponds to sulfur•••sulfur contact.

neighboring **A**, bridging the 1D arrangement of **A**. As a result, **A** and **B** formed a honeycomb-like two-dimensional (2D) lattice on a plane parallel to the (0 0 1) plane. The long axis and molecular plane of [Ni(dmit)$_2$]$^-$ **C** between the layers of the 2D honeycomb lattice are approximately parallel to the *a*-axis and to the (0 1 0) plane, respectively. Anion **C** is in contact with **A** and **B** between two S atoms, respectively. The supramolecular cations are aligned within the 1D channel extending in the [1 1 1] direction of the three-dimensional honeycomb lattice formed by [Ni(dmit)$_2$]$^-$.

The temperature dependence of **CE2A** occupancy is shown in Figure 2a. Although differential scanning calorimetry measurements did not detect any thermal anomalies between 180 and 300 K (Figure S3b), structural phases can be divided into three temperature regions corresponding to the disordered state of **CE2**. Between 113 and 133 K, the **CE2A** occupancy is almost independent of temperature, indicating that the **CE2** remains static within this range (113-143 K: Phase I). This static disorder in **CE2** transitions to a dynamic one above 143 K (143-193 K: Phase II). Indeed, temperature-frequency dependence of the dielectric constant shows a Debye-type relaxation over 150 K, with an activation energy of 9.58 kJ mol^{-1} (Figure S4). In Phase II, the twelve carbon atoms and six oxygen atoms comprising the [18]crown-6 molecules of **CE2A** or **CE2B** are almost in the same plane, suggesting that this dynamic disorder

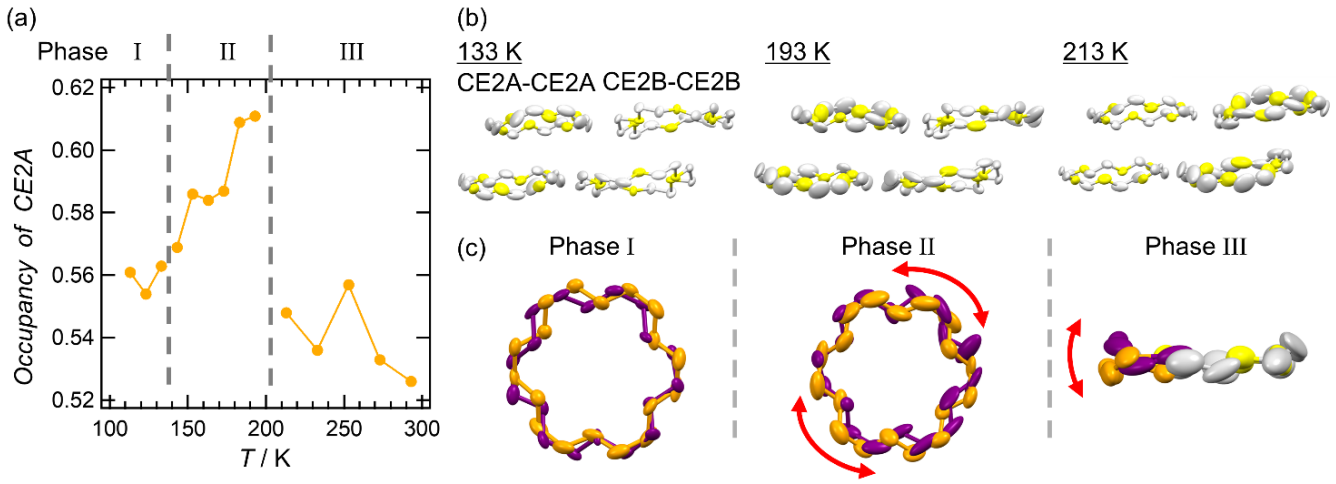

Figure 2. (a) Temperature dependence of **CE2A** occupancy. As there is a discontinuity between phases II and III, the conformer with the larger occupancy is denoted as **CE2A**. (b) Side views of disordered molecular pair of **CE2A** and **CE2B** in Phases I (133 K), II (193 K) and III (213 K). The carbon and oxygen atoms are shown in gray and yellow, respectively. Hydrogen atoms are omitted for clarity. (c) Disorder of **CE2** in each phase. **CE2A** and **CE2B** are shown in orange and purple, respectively. Carbon and oxygen atoms overlapping in phase III are shown in grey and yellow, respectively.

is characterized by in-plane molecular rotation (Figure 2c). As a result, the occupancy of **CE2A** changes significantly with temperature change. Above 213 K, out-of-plane disordering of the [18]crown-6 is also observed (213-293 K: Phase III). Three carbon atoms and one oxygen atom of the ethylene moiety of **CE2** deviate from the molecular mean plane of [18]crown-6 (Figure 2c). During the transition from Phase II to Phase III, the way the unit lattice was taken in X-ray crystallography changed (Figure S5 and Table S8).

The thermal expansion of crystal **1** from 113 to 293 K was analyzed based on the crystal structure. Since the crystal system of **1** is triclinic, it was converted to a Cartesian coordinate system using the *PASCal* program (Figure S6 in ESI).[30] The temperature dependence of the lengths of the principal axes $\boldsymbol{X_1}$, $\boldsymbol{X_2}$, and $\boldsymbol{X_3}$ is shown in Figure 3c. As indicated in Figure 3a and 3b, $\boldsymbol{X_1}$ is nearly orthogonal to the 1D chain of the supramolecular cation, while $\boldsymbol{X_2}$ and $\boldsymbol{X_3}$ are nearly orthogonal to the average planes of **CE1** and **CE2**, respectively. $\boldsymbol{X_2}$ and $\boldsymbol{X_3}$ exhibit PTE, whereas $\boldsymbol{X_1}$ shows NTE (Figure 3c). In all directions, CLTE behaved differently in three temperature regions: 113 - 133 K (Phase I) where **CE2** is static, 143 - 193 K (Phase II) where **CE2** rotates in-plane, and 213 - 293 K (Phase III) where **CE2** also moves out-of-plane. $\boldsymbol{X_1}$, which exhibits NTE, showed CLTE of -18×10^{-6} K^{-1} in Phase I, with minimal temperature fluctuations, whereas in Phase II, it showed a relatively large NTE with CLTE of -74×10^{-6} K^{-1}, which further accelerated to -105×10^{-6} K^{-1} in Phase III. The CLTE of $\boldsymbol{X_3}$, indicating PTE, was approximately four times higher than the CLTE of $\boldsymbol{X_2}$ over the entire temperature range. In all cases, discontinuities were observed across these temperature regions. The CLTE values are summarized in Table 1.

To comprehend the temperature-dependent behavior of the lengths of $\boldsymbol{X_1}$, $\boldsymbol{X_2}$, and $\boldsymbol{X_3}$, we focused on supramolecular cationic structure. Despite the flexible structure of the $(^{+}H_3N\text{-}C_2H_4)_2O$ cation, the intramolecular N1•••N2 atomic distance and N1•••O1•••N2 atomic angles are almost independent of temperature and the $(^{+}H_3N\text{-}C_2H_4)_2O$ cation structure remains almost unchanged in the temperature range from 113 to 293 K (Figure S7). Therefore, the $(^{+}H_3N\text{-}C_2H_4)_2O$ cation can be regarded as a rigid axle. On the other hand, the disordered state of **CE2** changes with increasing temperature, from static disorder in Phase I to dynamic one at temperatures above Phase II. Furthermore, in Phase III, out-of-plane motion of **CE2** is also observed. Relatively large rearrangement of the [18]crown-6 should contribute significantly to the CLTE of each axis.

Table 1. Coefficient of linear thermal expansion (CLTE) for $\boldsymbol{X_1}$, $\boldsymbol{X_2}$, and $\boldsymbol{X_3}$ in each phase.

Phase	Temperature range (K)	CLTE ($\times10^{-6}$ K^{-1})		
		$\boldsymbol{X_1}$	$\boldsymbol{X_2}$	$\boldsymbol{X_3}$
I	113 - 133	−18	48	101
II	143 - 193	−74	37	152
III	213 - 293	−105	35	194

Since $\boldsymbol{X_1}$ direction is nearly orthogonal to the 1D chain of the supramolecular cation (Figure 3a), tilt of [18]crown-6 molecules with respect to the 1D chain should be the origin of NTE seen in the temperature dependence of $\boldsymbol{X_1}$. The angles between the mean plane of **CE1**, **CE2A**, or **CE2B**, and the (1 1 1) (for 113 - 193 K) or (−1 1 1) (for 213 - 293 K) plane, which is approximately orthogonal to the direction of the 1D chain of supramolecular cations, is defined as $\boldsymbol{\Phi_{CE1}}$, $\boldsymbol{\Phi_{CE2A}}$ and $\boldsymbol{\Phi_{CE2B}}$, respectively. The temperature dependence of cos($\boldsymbol{\Phi_{CE1}}$, $\boldsymbol{\Phi_{CE2A}}$, and $\boldsymbol{\Phi_{CE2B}}$) corresponding to the distance in the $\boldsymbol{X_1}$ direction is shown in Figure 3d.

For all [18]crown-6 conformers, the slope in phase I is relatively small, while in phases II and III the slope increases with increasing temperature. This enhancement is particularly pronounced in the two **CE2** conformers, suggesting that these conformers determine $\boldsymbol{X_1}$. In fact, the average temperature dependence of cos($\boldsymbol{\Phi_{CE2A}}$) and cos($\boldsymbol{\Phi_{CE2B}}$), denoted as cos($\boldsymbol{\Phi_{CE2}}$),

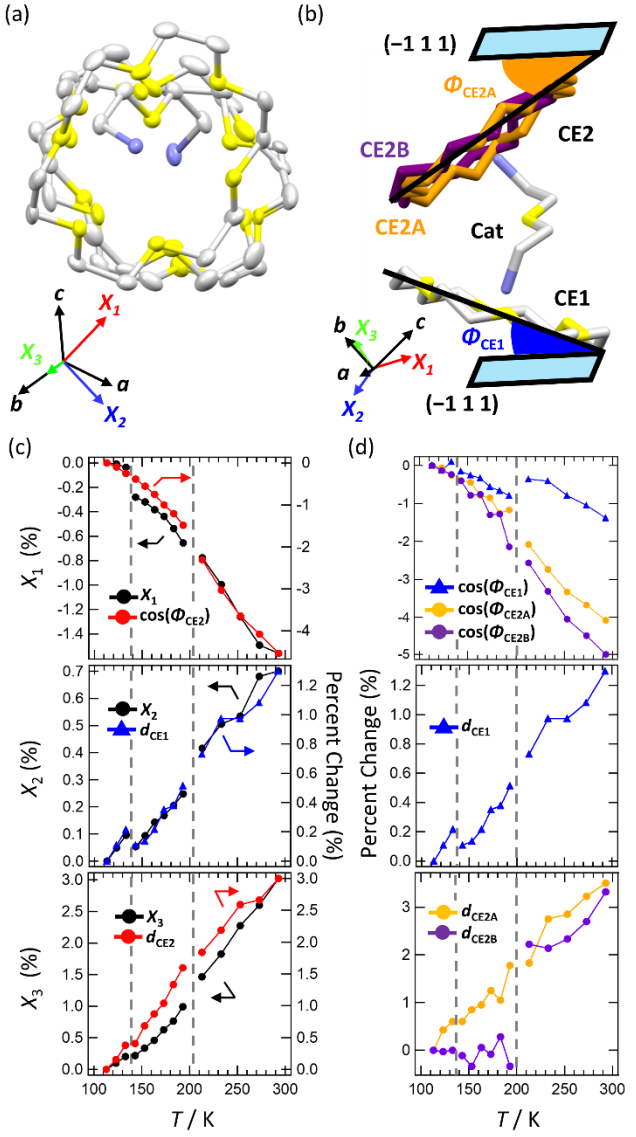

Figure 3. (a) Supramolecular cation viewed from the [1 1 1] direction at 113 K. (b) One-dimensional chain structure of supramolecular cation at 113 K. The angles between the mean plane of **CE1**, **CE2A** or **CE2B**, and (1 1 1) (for 113 - 193 K) or (−1 1 1) (for 213 - 293 K) plane are defined as Φ_{CE1}, Φ_{CE2A} and Φ_{CE2B} respectively. The Φ_{CE1} and Φ_{CE2A} are indicated by the red and orange fans, respectively. (c) Temperature dependence of the length of principal axes (X_1, X_2, X_3). Temperature dependence of the average values of cos(Φ_{CE2A}) and cos(Φ_{CE2B}), which is denoted as cos(Φ_{CE2}), d_{CE1}, and the average of d_{CE2A} and d_{CE2B} (denoted as d_{CE2}) are overlaid on those of X_1, X_2 and X_3, respectively. (d) Temperature dependence of cos(Φ_{CE2A}, Φ_{CE2B}, and Φ_{CE1}), d_{CE1}, d_{CE2A} and d_{CE2B} compared with each value at 113 K.

calculated considering the occupancy shown in Figure 2a, is consistent with the change in X_1 (Top in Figure 3c). CLTE of X_1 showing NTE is significantly accelerated as the state of **CE2** changed from static disorder, through in-plane rotation, to out-of-plane motion.

The X_2 and X_3, showing PTE, are approximately orthogonal to the mean planes of **CE1** and **CE2,** respectively (Figure 3b). The interplanar distances between the [18]crown-6 molecules are considered to determine X_2 and X_3. The average interplanar distances between nearest-neighbor [18]crown-6 molecules are plotted with reference to the values at 113 K (Figure 3d), Interplanar distance between **CE1•••CE1**, **CE2A•••CE2A** and **CE2B•••CE2B** are defined by the distance between average planes of adjacent molecules and denoted as d_{CE1}, d_{CE2A}, and d_{CE2B}, respectively. Since meshing between **CE2A•••CE2A** and **CE2B•••CE2B** pairs has been observed (Figure 2b and Table S2 in ESI), **CE2A•••CE2B** pairs, which do not involve inversion centers, were not considered as conformer combinations. The temperature dependence of these distances shows a discontinuity across phases, as in the case of X_2, and X_3. In **CE1•••CE1** pairs where no molecular motion was observed, d_{CE1} increased monotonically and showed an increase of about 1% between 113 and 293 K. The temperature-dependent trend of d_{CE1} almost exactly reproduces that of X_2 (middle in Figure 3c), suggesting a strong relationship between d_{CE1} and X_2.

The elongation of d_{CE2} over the entire temperature range is about four times that of d_{CE1}, which corresponds to a CLTE in the X_3 direction of about four times that of X_2. The temperature dependence of the interplanar distance of **CE2** varied significantly depending on the combination of **CE2A** and **CE2B**.

While d_{CE2A} showed a monotonic increase over the entire temperature range, d_{CE2B} showed a complex temperature dependence, with large jumps at the boundary between phases II and III (Bottom in Figure 3d). However, as in the case of X_1, the average of d_{CE2A} and d_{CE2B} (denoted as d_{CE2}) calculated taking occupancy into account, reproduced the monotonic temperature variation of X_3 well (bottom in Figure 3c). The tilt of the [18]crown-6 **CE2** with respect to the 1D chain contributes mainly to the NTE in the X_1 direction orthogonal to the chain, and the change in distance between each pair of **CE1** and **CE2** determines the X_2 and X_3, respectively.

[18]crown-6 has no aromatic rings and the intermolecular interactions are relatively weak. The degree of molecular rearrangement in the crystal is therefore relatively larger than in crystals with benzo[18]crown-6 or dibenzo[24]crown-8. As a result, uniaxial NTE above -100×10^{-6} K^{-1} is achieved in crystal **1**, which is greater than those of (4-amionopyridinium$^+$)(benzo[18]crown-6)[Ni(dmit)$_2$]$^-$ (197-282 K: -72.1×10^{-6} K^{-1}) and (pyridazinium$^+$)$_2$(dibenzo[24]crown-8)$_3$[Ni(dmit)$_2$]$^-_2$ (186-282 K: -81.3×10^{-6} K^{-1}) crystals.[28,29]

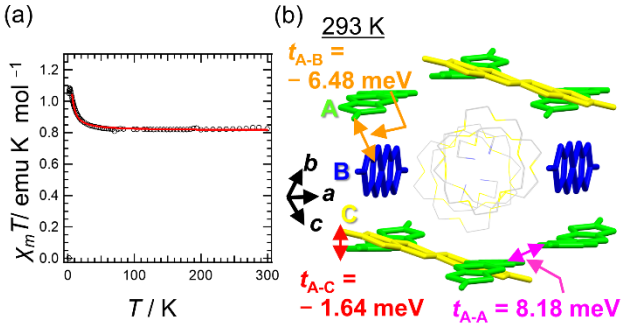

Figure 4. (a) Temperature dependence of the molar magnetic susceptibility of crystal **1** ($\chi_m T$ versus T plot). The red line is a fit by the Curie-Weiss law (see text). (b) Transfer integrals between [Ni(dmit)$_2$]$^-$ in crystal **1** at 293 K.

The temperature dependence of molar magnetic susceptibility (χ_m) is shown in Figure 4a, where the temperature dependence of χm is reproduced by the Curie-Weiss low with the Curie constant of 0.813 cm^3 K mol^{-1} and the Weiss temperature (ϑ) of +1.41 K. Positive value of ϑ indicates that the $[Ni(dmit)_2]^-$ anions are ferromagnetically coupled. Figure 4b depicts the transfer integrals (t) between two $[Ni(dmit)_2]^-$ anions; the calculated t for the **A•••A**, **A•••B**, and **A•••C** interactions, which are denoted as $t_{A\text{-}A}$, $t_{A\text{-}B}$, and $t_{A\text{-}C}$, are 8.18, −6.48, and −1.64 meV, respectively. The single occupied molecular orbital of $[Ni(dmit)_2]^-$ was nearly orthogonal to the orbitals of the neighboring $[Ni(dmit)_2]^-$, which is in good agreement with the result that the $[Ni(dmit)_2]^-$ anions are ferromagnetically coupled to each other.[31–34]

Conclusions

Multi-step negative thermal expansion (NTE) is achieved on the basis of the change in molecular motion modes of wheel-axle-type supramolecular cation formed by [18]crown-6 and $(^+H_3N\text{-}C_2H_4)_2O$ in crystal by utilizing a supramolecular approach. Within the crystal, $(^+H_3N\text{-}C_2H_4)_2O$ and [18]crown-6 acted as a rigid axle and wheels, respectively, forming one-dimensional (1D) chains. The tilt of the [18]crown-6 **CE2** with respect to the 1D chain mainly caused NTE. With increasing temperature, **CE2** changed its disorder state from static disorder to out-of-plane motion via in-plane rotation, resulting in a multi-step enhancement of the uniaxial NTE. In particular, coefficient of linear thermal expansion in the $\boldsymbol{X_1}$ axis, which shows NTE, exceeded -100×10^{-6} K^{-1} in the temperature region where [18]crown-6 exhibits out-of-plane disorder. This value was the largest among the $[Ni(dmit)_2]^-$ salts designed on the basis of the supramolecular approach reported so far. Ferromagnetic interactions were observed between $[Ni(dmit)_2]^-$ forming a honeycomb structure. The use of molecular motion is a powerful method of acquiring entropy unique to molecular crystals. Changes in the mode of molecular motion in supramolecular structures offers new possibilities for multi-step control of thermal expansion. Molecular motion based on the supramolecular approach can also be coupled with the electrical and magnetic properties exhibited by crystals, which is expected to open up functional hybrid materials with controlled thermal expansion.

Author contributions

M. H. and N. H. performed the synthesis of compound **1** under the guidance of J. W., K. T., R. H., and C. X.
M. H. and S. N. acquired and analysed the thermal data. M. H and K. T. performed the crystallography, and acquired, analysed, and interpreted the magnetic data. M. H., K. T., and T. N. conceived and compiled the idea for the research and analysed and interpreted all data. The first manuscript was written by M. H., K. T. and T. N. and edited by all authors.

Data availability

The crystallographic data (CIF files) for the structures reported in this article have been deposited with the Cambridge Crystallographic Data Centre (CCDC), under deposition numbers 2384649, 2384650, 2384651, 2384652, 2384653, 2384654, 2384655, 2384656, 2384657, 2384658, 2384659, 2384660, 2384661, and 2384662 for crystal **1** at 113, 123, 133,143, 153, 163, 173, 183, 193, 213, 233, 253, 273, and 293 K, respectively. These data can be obtained free of charge via www.ccdc.cam.ac.uk/data_request/cif, or by emailing data_request@ccdc.cam.ac.uk, or by contacting The Cambridge Crystallographic Data Centre, 12 Union Road, Cambridge CB2 1EZ, UK; fax: +44 1223 336033. All experimental data within the article and its ESI† are available from the corresponding authors upon requested.

Conflicts of interest

There are no conflicts to declare.

Acknowledgements

The authors thank Ai Tokumitsu of the Global Facility Center, Hokkaido University, for elemental analysis and Dr. Shuhei Fukuoka and Dr. Satoaki Matsunaga of the Faculty of Science, Hokkaido University, for χ_m measurements. This study was financially supported by JSPS KAKENHI (grant no. JP22H00311), JST ACT-X (grant no. JPMJAX23DB), the research project of "Crossover Alliance to Create the Future with People, Intelligence and Materials", and Research Program of "Network Joint Research Center for Materials and Devices", from the Ministry of Education, Culture, Sports, Science and Technology of Japan (MEXT). This research was also supported financially by the Iketani Science and Technology Foundation.

Notes and references

1 Q. Liu, J. Yang, X. Cheng, G. Liang and X. Sun, *Ceramics International*, 2012, **38**, 541–545.
2 Y. Okahisa, A. Yoshida, S. Miyaguchi and H. Yano, *Composites Science and Technology*, 2009, **69**, 1958–1961.
3 X. Ge, Y. Mao, X. Liu, Y. Cheng, B. Yuan, M. Chao and E. Liang, *Sci Rep*, 2016, **6**, 24832.
4 Th. B. Singh, F. Meghdadi, S. Günes, N. Marjanovic, G. Horowitz, P. Lang, S. Bauer and N. S. Sariciftci, *Advanced Materials*, 2005, **17**, 2315–2320.
5 X. Yang, X. Cheng, X. Yan, J. Yang, T. Fu and J. Qiu, *Composites Science and Technology*, 2007, **67**, 1167–1171.
6 Z. Liu, Q. Gao, J. Chen, J. Deng, K. Lin and X. Xing, *Chem. Commun.*, 2018, **54**, 5164–5176.
7 A. L. Goodwin and C. J. Kepert, *Phys. Rev. B*, 2005, **71**, 140301.
8 K. W. Chapman, P. J. Chupas and C. J. Kepert, *J. Am. Chem. Soc.*, 2005, **127**, 15630–15636.
9 S. J. Hibble, A. M. Chippindale, E. Marelli, S. Kroeker, V. K. Michaelis, B. J. Greer, P. M. Aguiar, E. J. Bilbé, E. R. Barney and A. C. Hannon, *J. Am. Chem. Soc.*, 2013, **135**, 16478–16489.
10 D. J. Williams, D. E. Partin, F. J. Lincoln, J. Kouvetakis and M. O'Keeffe, *Journal of Solid State Chemistry*, 1997, **134**, 164–169.

11 A. E. Phillips, A. L. Goodwin, G. J. Halder, P. D. Southon and C. J. Kepert, *Angewandte Chemie International Edition*, 2008, **47**, 1396–1399.
12 A. E. Phillips, G. J. Halder, K. W. Chapman, A. L. Goodwin and C. J. Kepert, *J. Am. Chem. Soc.*, 2010, **132**, 10–11.
13 D. Das, T. Jacobs and L. J. Barbour, *Nature Mater*, 2010, **9**, 36–39.
14 M. K. Panda, T. Runčevski, S. Chandra Sahoo, A. A. Belik, N. K. Nath, R. E. Dinnebier and P. Naumov, *Nat Commun*, 2014, **5**, 4811.
15 K. Wang, H. Zhang, S. Chen, G. Yang, J. Zhang, W. Tian, Z. Su and Y. Wang, *Advanced Materials*, 2014, **26**, 6168–6173.
16 M. Brinkmann, G. Gadret, M. Muccini, C. Taliani, N. Masciocchi and A. Sironi, *J. Am. Chem. Soc.*, 2000, **122**, 5147–5157.
17 R. H. Jones, K. S. Knight, W. G. Marshall, J. Clews, R. J. Darton, D. Pyatt, S. J. Coles and P. N. Horton, *CrystEngComm*, 2013, **16**, 237–243.
18 L. Yu, *Acc. Chem. Res.*, 2010, **43**, 1257–1266.
19 C. G. Salzmann, P. G. Radaelli, B. Slater and J. L. Finney, *Phys. Chem. Chem. Phys.*, 2011, **13**, 18468–18480.
20 R. Ohtani, A. Grosjean, R. Ishikawa, R. Yamamoto, M. Nakamura, J. K. Clegg and S. Hayami, *Inorg. Chem.*, 2017, **56**, 6225–6233.
21 R. Ohtani, J. Yanagisawa, B. Le Ouay and M. Ohba, *ChemNanoMat*, 2021, **7**, 534–538.
22 N. Lock, Y. Wu, M. Christensen, L. J. Cameron, V. K. Peterson, A. J. Bridgeman, C. J. Kepert and B. B. Iversen, *J. Phys. Chem. C*, 2010, **114**, 16181–16186.
23 J. P. Attfield, *Front. Chem.*, 2018, **6**, 371.
24 D. Wendt, E. Bozin, J. Neuefeind, K. Page, W. Ku, L. Wang, B. Fultz, A. V. Tkachenko and I. A. Zaliznyak, *Science Advances*, 2019, **5**, eaay2748.
25 Z.-K. Liu, Y. Wang and S. Shang, *Sci Rep*, 2014, **4**, 7043.
26 B. Mu and K. S. Walton, *J. Phys. Chem. C*, 2011, **115**, 22748–22754.
27 Z.-S. Yao, M. Mito, T. Kamachi, Y. Shiota, K. Yoshizawa, N. Azuma, Y. Miyazaki, K. Takahashi, K. Zhang, T. Nakanishi, S. Kang, S. Kanegawa and O. Sato, *Nature Chem*, 2014, **6**, 1079–1083.
28 K. Takahashi, Y. Shirakawa, H. Sakai, I. Hisaki, S. Noro, T. Akutagawa, M. Nakano and T. Nakamura, *J. Mater. Chem. C*, 2023, **11**, 1891–1898.
29 S. Li, K. Takahashi, R.-K. Huang, C. Xue, K. Kokado, N. Hoshino, T. Akutagawa, S. Nishihara and T. Nakamura, *Chem. Mater.*, 2023, **35**, 2421–2428.
30 M. J. Cliffe and A. L. Goodwin, *J Appl Cryst*, 2012, **45**, 1321–1329.
31 K. Awaga, T. Sugano and M. Kinoshita, *Chemical Physics Letters*, 1987, **141**, 540–544.
32 J. Nishijo, S. Numao, K. Judai and N. Nishi, *Polyhedron*, 2009, **28**, 1664–1667.
33 T. Akutagawa, D. Sato, Q. Ye, S. Noro and T. Nakamura, *Dalton Trans.*, 2010, **39**, 2191–2193.
34 T. Akutagawa, D. Sato, H. Koshinaka, M. Aonuma, S. Noro, S. Takeda and T. Nakamura, *Inorg. Chem.*, 2008, **47**, 5951–5962.

Supporting Information

Three-Step Change in Uniaxial Negative Thermal Expansion by Switching Supramolecular Motion Modes in Ferromagnetically-Coupled Nickel Dithiolate Lattice

Masato Haneda, Kiyonori Takahashi,* Naohiro Hasuo, Rui-Kang Huang, Chen Xue, Jia-bing Wu, Shin-ichiro Noro, and Takayoshi Nakamura*

E-mail: ktakahashi@es.hokudai.ac.jp (K. Takahashi), tnaka@es.hokudai.ac.jp (T. Nakamura)

§Experimental Section

General.

All reagents purchased were used without further purification. Elemental analyses were carried out by using a CHN analyzer (CE440, Exeter Analytical, Inc.) at Global Facility Center, Hokkaido University.

Synthesis.

Precursor of $(TBA^+)[Ni(dmit)_2]^-$ (TBA^+= tetra-*n*-butylammonium$^+$) was prepared using a procedure reported in the literature.[S1] A 42 % HBF_4 (602 mg, 2.88 mmol) was added to a solution of 2,2'-oxybis(ethylamine) (407 mg, 1.44 mmol) in CH_3CN (2 mL). The mixture solution was stirred at r.t. for 1 h. The solvent was removed under reduced pressure to obtain a white solid. The solid was recrystallized by $CHCl_3/CH_3OH$ to obtain a $(({}^+H_3N\text{-}C_2H_4)_2O)(BF_4^-)_2$. A solution of $(TBA^+)[Ni(dmit)_2]^-$ (20 mg, 0.04 mmol) in CH_3CN (20 mL) was added to a solution of [18]crown-6 (94 mg, 0.35 mmol) and $(({}^+H_3N\text{-}C_2H_4)_2O)(BF_4^-)_2$ (37 mg, 0.13 mmol) in CH_3CN (19 mL) and CH_3OH (1 mL). Crystal **1** was obtained by slow diffusion over a period of 4 days. Elemental analysis for crystal **1**: calcd. for $C_{40}H_{62}N_2Ni_2O_{13}S_{20}$: C: 31.25%, H: 4.06%, N: 1.82%, Found : C: 30.97%, H: 3.93%, N: 1.73%.

Crystal structure determination.

Temperature-dependent structural analysis of the single crystal **1** was performed using a Rigaku XtaLAB-Synergy diffractometer with a HyPix-6000 area detector and multilayer mirror-monochromated Mo Kα radiation (λ = 0.71073 Å). A single

crystal was mounted on a MicroMountsTM tip (MiTeGen) with Paratone 8277 (Hampton Research). The temperature dependence was measured using the same crystal. For the reflection data, multi-scan absorption corrections were applied to the crystal. Data collection was performed and processed using the CrysAlisPRO interface (Oxford Diffraction, Agilent Technologies UK Ltd). The initial structure was solved using SHELXT,[S2] and structural refinement was performed using OLEX2 software.[S3] Anisotropic refinement was applied to all atoms, except for the hydrogen atoms. Cif files are deposited in Cambridge The Cambridge Crystallographic Data Centre (CCDC) with CCDC numbers 2384649, 2384650, 2384651, 2384652, 2384653, 2384654, 2384655, 2384656, 2384657, 2384658, 2384659, 2384660, 2384661, and 2384662 for crystal **1** at 113, 123, 133,143, 153, 163, 173, 183, 193, 213, 233, 253, 273, and 293 K, respectively. The CLTE was calculated using the *PASCal* web program based on the unit cell parameters at each temperature.[S4]

Physical Property Measurements.

Differential scanning calorimetry (DSC) measurements were carried out using a Q2000 differential scanning calorimeter (TA Instruments) in the temperature range from 180 to 300 K at a scanning rate of 5 K min^{-1} under a flow of N_2 gas (50 mL min^{-1}). Temperature- and frequency-dependence of dielectric constant was measured using an impedance analyzer 4294A (Agilent) with the four-probe AC impedance method at a frequency range of 10^3–10^4 Hz. The temperature was controlled using cryostats with temperature controller models 331 (Lake Shore Cryotronics Inc.). Electrical contacts were prepared using a silver paste (D-500,

Fujikura Kasei Co.,Ltd.) to attach the 25 μm ϕ gold wires to the single crystal. The temperature-dependent molar magnetic susceptibility (χ_m) for polycrystalline sample of **1** was measured using a Quantum Design MPMS-3 SQUID magnetometer. Prior to sample measurement, the magnetic susceptibility of the sample holder (aluminum film) was measured under identical conditions, then the susceptibility of the holder was subtracted from the gram susceptibility as the paramagnetic contribution. The diamagnetic component in the sample was subtracted based on Pascals constant, -7.1674×10^{-4} cm^3 mol^{-1}.[S5] A magnetic field of 1 T was applied for all temperature-dependent measurements. Molecular weight of 1537.52 g mol^{-1} (the χ_m for two $[Ni(dmit)_2]^-$ molecules) was used for calculation of χ_m of crystal **1**.

Theoretical calculation

The extended Hückel molecular orbital method within the tight-binding approximation was applied to calculate the transfer integral (*t*) data between the $[Ni(dmit)_2]^-$ anions in crystal **1**. The lowest unoccupied molecular orbital of the $[Ni(dmit)_2]^-$ molecule was used as the basis function. According to the literature, semiempirical parameters for Slater-type atomic orbitals were obtained.[S6] The *t* values between each pair of molecules were assumed to be proportional to the overlap integral (*S*) according to the equation $t = -10S$ (eV).

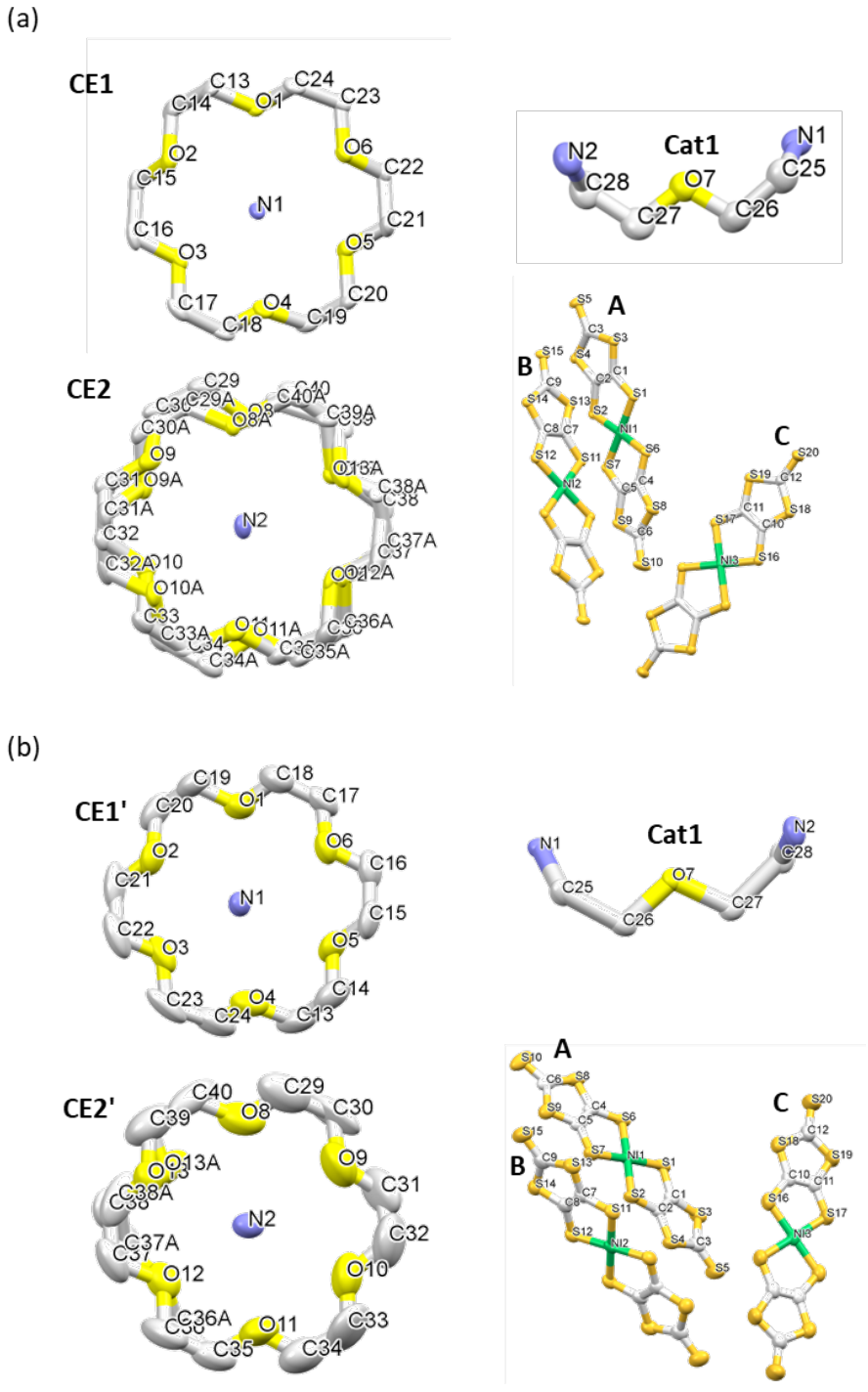

§Figure S1. Crystallographically independent structures of crystal **1** at 113 K (a) and 213 K (b). The Ni, S, C, N, and O atoms are depicted in green, orange, gray, blue, and yellow, respectively. All molecules are depicted as ellipsoid models. Hydrogen atoms are omitted for clarity.

§Table S1. Distances and angles for N-H•••O hydrogen bonding.

	Contacted atoms					
	N1-H1B•••O1			N1-H1C•••O3		
T **/ K**	**N•••O distance(Å)**	**H•••O distance(Å)**	**N-H•••O angle(°)**	**N•••O distance(Å)**	**H•••O distance(Å)**	**N-H•••O angle(°)**
113	2.881(3)	2.019	157.700	2.911(4)	2.085	150.5
123	2.881(3)	2.017	158.070	2.91(4)	2.083	150.56
133	2.883(3)	2.018	158.260	2.912(4)	2.085	150.49
143	2.881(3)	2.023	156.730	2.909(4)	2.086	149.8
153	2.880(3)	2.023	156.550	2.91(4)	2.087	149.73
163	2.883(3)	2.028	155.910	2.912(4)	2.093	149.11
173	2.883(3)	2.035	154.500	2.913(4)	2.098	148.44
183	2.881(4)	2.029	155.280	2.913(4)	2.095	148.92
193	2.881(4)	2.039	153.230	2.916(4)	2.106	147.76
213	2.918(6)	2.111	148.730	2.888(5)	2.044	155.88
233	2.917(4)	2.122	146.840	2.885(4)	2.055	152.88
253	2.920(4)	2.130	145.910	2.887(4)	2.068	150.9
273	2.924(5)	2.144	145.910	2.892(5)	2.081	151.07
293	2.916(5)	2.138	145.760	2.898(5)	2.086	151.34

	Contacted atoms					
	N1-H1A•••O5			N2-H2C•••O8		
T **/ K**	**N•••O distance(Å)**	**H•••O distance(Å)**	**N-H•••O angle(°)**	**N•••O distance(Å)**	**H•••O distance(Å)**	**N-H•••O angle(°)**
113	2.917(4)	2.04	161.4	2.99(2)	2.15	154.8
123	2.918(4)	2.039	161.96	2.987(2)	2.143	153.68
133	2.92(4)	2.041	162.18	2.973(2)	2.136	152.52
143	2.914(4)	2.039	160.87	2.987(2)	2.146	153.32
153	2.914(4)	2.039	160.91	2.973(2)	2.13	153.73
163	2.917(4)	2.043	160.63	2.989(2)	2.152	152.54
173	2.917(4)	2.049	159.12	2.994(2)	2.18	148.58
183	2.917(4)	2.046	159.77	2.979(2)	2.158	149.53
193	2.917(4)	2.054	157.79	2.988(2)	2.187	146.5
213	2.919(5)	2.056	160.33	2.946(7)	2.178	142.96
233	2.927(4)	2.075	157.47	2.954(6)	2.19	142.26
253	2.927(4)	2.082	156.02	2.948(6)	2.207	139.3
273	2.932(5)	2.097	155.71	2.954(6)	2.211	140.68

293	2.925(5)	2.086	156.61	2.952(6)	2.216	139.73

Contacted atoms

	N2-H2A•••O10			N2-H2B•••O12		
T **/ K**	**N•••O distance(Å)**	**H•••O distance(Å)**	**N-H•••O angle(°)**	**N•••O distance(Å)**	**H•••O distance(Å)**	**N-H•••O angle(°)**
113	2.918(9)	2.112	147.1	2.88(2)	2.02	158.8
123	2.924(1)	2.122	146.32	2.888(2)	2.022	158.42
133	2.948(1)	2.151	145.67	2.824(2)	1.959	157.99
143	2.945(1)	2.147	145.88	2.884(2)	2.024	156.97
153	2.948(1)	2.15	146.04	2.893(2)	2.036	156.22
163	2.958(1)	2.165	145.14	2.886(3)	2.032	155.67
173	2.95(1)	2.177	142.42	2.929(2)	2.08	154.75
183	2.971(1)	2.189	143.62	2.924(3)	2.088	152.34
193	2.984(1)	2.215	141.82	2.89(2)	2.066	150.09
213	2.919(7)	2.097	151.31	2.881(5)	2.089	146.44
233	2.918(7)	2.103	150.12	2.891(5)	2.105	145.34
253	2.923(7)	2.13	146.59	2.895(5)	2.138	141.19
273	2.892(7)	2.081	151.07	2.889(5)	2.128	142.93
293	2.898(7)	2.086	151.34	2.90(5)	2.149	141.57

Contacted atoms

	N2-H2C•••O8A			N2-H2A•••O10A		
T **/ K**	**N•••O distance(Å)**	**H•••O distance(Å)**	**N-H•••O angle(°)**	**N•••O distance(Å)**	**H•••O distance(Å)**	**N-H•••O angle(°)**
113	2.74(2)	1.86	160.5	2.94(1)	2.06	163
123	2.761(2)	1.89	159.56	2.929(1)	2.048	162.49
133	2.767(2)	1.9	158.45	2.915(1)	2.036	161.83
143	2.742(2)	1.876	158.38	2.905(1)	2.027	161.8
153	2.756(2)	1.888	158.71	2.90(2)	2.021	161.9
163	2.741(2)	1.878	157.65	2.889(2)	2.017	160.21
173	2.728(2)	1.877	154.72	2.895(2)	2.027	158.94
183	2.75(3)	1.896	155.22	2.866(2)	1.994	159.84
193	2.743(3)	1.903	152.66	2.868(2)	2.005	157.59

	Contacted atoms		
	N2-H2B•••O12A		
T **/ K**	**N•••O distance(Å)**	**H•••O distance(Å)**	**N-H•••O angle(°)**
113	2.95(2)	2.07	159.9
123	2.945(2)	2.077	159.16
133	3.008(2)	2.146	157.75
143	2.95(2)	2.079	159.75
153	2.93(4)	2.052	161.68
163	2.946(3)	2.071	161.01
173	2.894(3)	2.039	156.04
183	2.885(4)	2.01	161.03
193	2.929(4)	2.064	158.51

§Table S2. Distances and angles for C-H•••O interactions between crown ethers at 113 and 143 K.

Contacted units	list of atoms	C•••O distance	H•••O distance	C-H•••O angle
113 K				
CE1•••CE1	C16-H16B•••O1	3.570(5)	2.666	152.04
CE1•••CE1	C17-H17A•••O5	3.628(6)	2.796	142.04
CE2A•••CE2A	[a] C40A-H40D•••O9A	3.66(2)	2.794	146
CE2B•••CE2B	C40A-H40D•••O9A	3.61(1)	2.743	146.7
CE2A•••CE2A	C29A-H29A•••O13A	3.61(1)	2.764	143.6
143 K				
CE1•••CE1	[a] C16-H16B•••O1	3.576(5)	2.672	152
CE2A•••CE2A	C30-H30B•••O12	3.89(3)	2.987	145
CE2A•••CE2A	C39-H39A•••O10	3.66(2)	2.805	152
CE2B•••CE2B	C40A-H40D•••O9A	3.61(1)	2.734	147.9
CE2B•••CE2B	C29A-H29C•••O13A	3.62(1)	2.775	143.2

[a] C-H•••O interactions in a complementary manner.

§Table S3. Distance between sulfur•••sulfur atoms less than the sum of the van der Waals radii of two sulfur between two [Ni(dmit)$_2$] anions.

	Contacted units				
	A•••A		**A•••B**	**A•••C**	**B•••C**
	Distance between contacted atoms / Å				
***T* / K**	S7•••S9	S7•••S7	S3•••S14	S1•••S18	S12•••S18
113	3.45(1)	3.43(1)	3.637(1)	3.563(2)	3.573(2)
123	3.452(2)	3.435(1)	3.638(2)	3.568(2)	3.575(2)
133	3.457(2)	3.441(1)	3.639(2)	3.575(2)	3.577(2)
143	3.455(2)	3.444(1)	3.636(2)	3.576(2)	3.572(2)
153	3.459(2)	3.449(1)	3.638(2)	3.583(2)	3.574(2)
163	3.462(2)	3.454(1)	3.638(2)	3.59(2)	3.574(2)
173	3.468(2)	3.46(1)	3.642(2)	3.599(2)	3.575(2)
183	3.469(2)	3.466(1)	3.644(2)	3.609(2)	3.575(2)
193	3.475(2)	3.473(1)	3.645(2)	3.621(2)	3.576(2)
	Distance between contacted atoms / Å				
	S6•••S8	S6•••S6	S6•••S13	S5•••S14	S14•••S19
213	3.489(2)	3.491(2)	3.637(2)	3.835(2)	3.581(2)
233	3.50(2)	3.503(1)	3.651(2)	3.837(2)	3.58(2)
253	3.507(2)	3.517(1)	3.662(2)	3.838(2)	3.579(2)
273	3.508(2)	3.523(1)	3.67(2)	3.844(2)	3.579(2)
293	3.52(2)	3.538(1)	3.679(2)	3.849(2)	3.586(2)

§Table S4. Distances and angles for C-H•••S interactions between cation and anion **C**.

	Contacted atoms C27-H27A•••S19		
***T* / K**	**C•••S distance(Å)**	**H•••S distance(Å)**	**C-H•••S angle(°)**
113	3.735(5)	2.852	148.96
123	3.74(5)	2.858	148.8
133	3.742(5)	2.857	149.18
143	3.74(5)	2.853	149.39
153	3.743(5)	2.854	149.71
163	3.749(5)	2.862	149.47
173	3.753(5)	2.863	149.92
183	3.755(5)	2.865	149.98
193	3.764(5)	2.871	150.32
	Contacted atoms C27-H27B•••S16		
	C•••S distance(Å)	**H•••S distance(Å)**	**C-H•••S angle(°)**
213	3.781(5)	2.897	150.45
233	3.798(5)	2.91	151.13
253	3.804(5)	2.914	151.48
273	3.82(5)	2.938	151.83
293	3.831(5)	2.945	152.32

§Table S5. Distances and angles for C-H•••C interactions between cation and anion **C**.

		Contacted atoms C27-H27A•••C11	
***T* / K**	**C•••C distance(Å)**	**H•••C distance(Å)**	**C-H•••C angle(°)**
113	3.765(6)	2.82	159.84
123	3.765(6)	2.821	159.81
133	3.764(6)	2.819	159.69
143	3.759(6)	2.816	159.42
153	3.757(6)	2.814	159.35
163	3.758(6)	2.814	159.45
173	3.759(6)	2.817	159.19
183	3.754(6)	2.811	159.41
193	3.757(6)	2.815	159.13
		Contacted atoms C27-H27B•••C10	
	C•••C distance(Å)	**H•••C distance(Å)**	**C-H•••C angle(°)**
213	3.754(6)	2.818	159.8
233	3.76(6)	2.823	160.09
253	3.752(6)	2.818	159.51
273	3.761(6)	2.836	159.86
293	3.766(6)	2.836	160.78

§Table S6. Distances and angles for C-H•••S interactions between **CE1** and anion **A**.

	Contacted atoms					
	C18-H18B•••S2			C20-H20A•••S10		
T **/ K**	**C•••S distance(Å)**	**H•••S distance(Å)**	**C-H•••S angle(°)**	**C•••S distance(Å)**	**H•••S distance(Å)**	**C-H•••S angle(°)**
113	3.849(4)	2.966	149.08	3.749(5)	2.853	150.8
123	3.851(4)	2.97	148.92	3.75(5)	2.852	151.1
133	3.858(4)	2.974	149.28	3.747(5)	2.85	151.01
143	3.852(4)	2.971	148.85	3.738(5)	2.843	150.64
153	3.855(4)	2.974	148.83	3.737(5)	2.841	150.67
163	3.859(5)	2.981	148.33	3.737(5)	2.843	150.5
173	3.865(5)	2.985	148.62	3.731(5)	2.84	150.11
183	3.864(5)	2.984	148.63	3.728(5)	2.837	150.11
193	3.864(5)	2.982	148.95	3.728(5)	2.836	150.18
	Contacted atoms					
	C23-H23A•••S4			C21-H21B•••S10		
	C•••S distance(Å)	**H•••S distance(Å)**	**C-H•••S angle(°)**	**C•••S distance(Å)**	**H•••S distance(Å)**	**C-H•••S angle(°)**
213	3.869(6)	2.994	149.29	3.718(7)	2.842	149.2
233	3.872(6)	2.996	149.49	3.718(6)	2.845	148.87
253	3.883(7)	3.006	149.54	3.711(6)	2.842	148.35
273	3.882(7)	3.011	150.09	3.706(6)	2.857	146.68
293	3.888(7)	3.018	149.82	3.706(6)	2.857	146.64

§Table S7. Distances and angles for C-H•••S interactions between **CE2** and anion **A**.

	Contacted atoms					
	C32-H32B•••S10			C35-H35B•••S6		
T **/ K**	**C•••S distance(Å)**	**H•••S distance(Å)**	**C-H•••S angle(°)**	**C•••S distance(Å)**	**H•••S distance(Å)**	**C-H•••S angle(°)**
113	3.71(2)	2.983	131.11	3.687(2)	2.81	148.05
123	3.709(2)	2.98	131.32	3.683(2)	2.804	148.29
133	3.711(2)	2.99	130.53	3.694(2)	2.808	149.17
143	3.704(2)	2.984	130.54	3.677(2)	2.792	149.06
153	3.691(2)	2.952	132.21	3.665(2)	2.795	146.89
163	3.699(2)	2.967	131.63	3.665(3)	2.796	146.76
173	3.696(2)	2.961	131.88	3.659(3)	2.764	150.62
183	3.707(2)	2.988	130.41	3.665(3)	2.784	148.56
193	3.702(2)	2.964	132.16	3.674(3)	2.767	152.41
	Contacted atoms					
	C40-H40B•••S10			C36-H36B•••S3		
	C•••S distance(Å)	**H•••S distance(Å)**	**C-H•••S angle(°)**	**C•••S distance(Å)**	**H•••S distance(Å)**	**C-H•••S angle(°)**
213	3.72(8)	2.929	138.54	3.348(1)	2.676	126.09
233	3.738(8)	2.95	138.24	3.349(1)	2.656	127.93
253	3.738(7)	2.944	138.83	3.364(1)	2.692	126.19
273	3.754(8)	2.976	138.21	3.359(1)	2.689	126.67
293	3.762(8)	2.97	139.62	3.369(2)	2.684	128

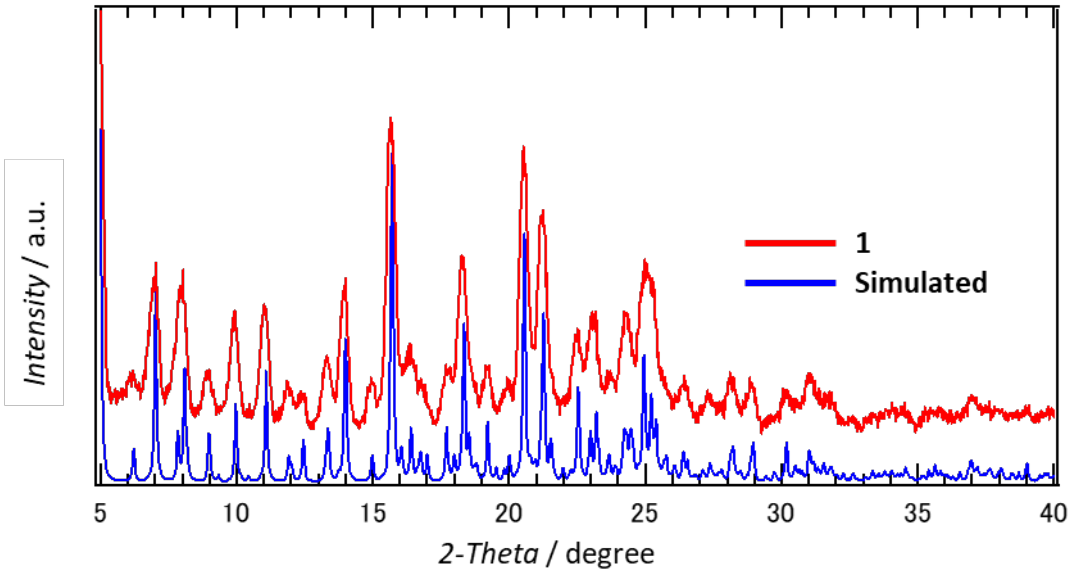

§Figure S2. Powder X-ray diffraction (PXRD) pattern of crystal **1** measured at room temperature. Simulated patterns were compared with the experimental ones to confirm purity of the sample.

PXRD pattern are measured with a Rigaku RINT2113 in the 2θ region of 5-40°. The measurements were performed with CuK_{α} radiation (λ = 1.5418 Å) at scanning rate of 1.2°•min^{-1} under an applied electric voltage and current of 40 KV and 40 mA, respectively.

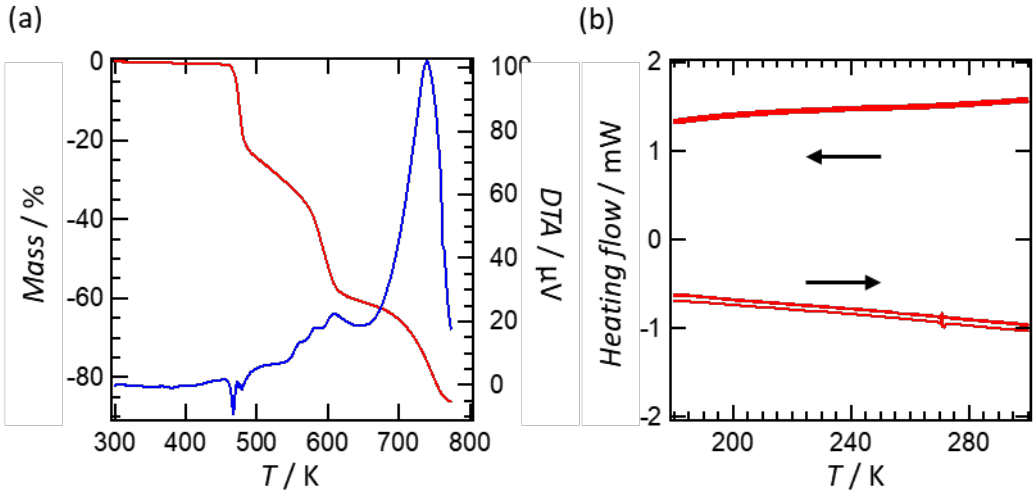

§Figure S3. (a) TG-DTA measurement for crystal **1**. (b) DSC from 180 to 300 K. Thermogravimetric-differential thermal analysis (TG-DTA) was conducted using a *Rigaku* Thermo Plus TG8120 with 10 K/min heating rate under nitrogen gas flow.

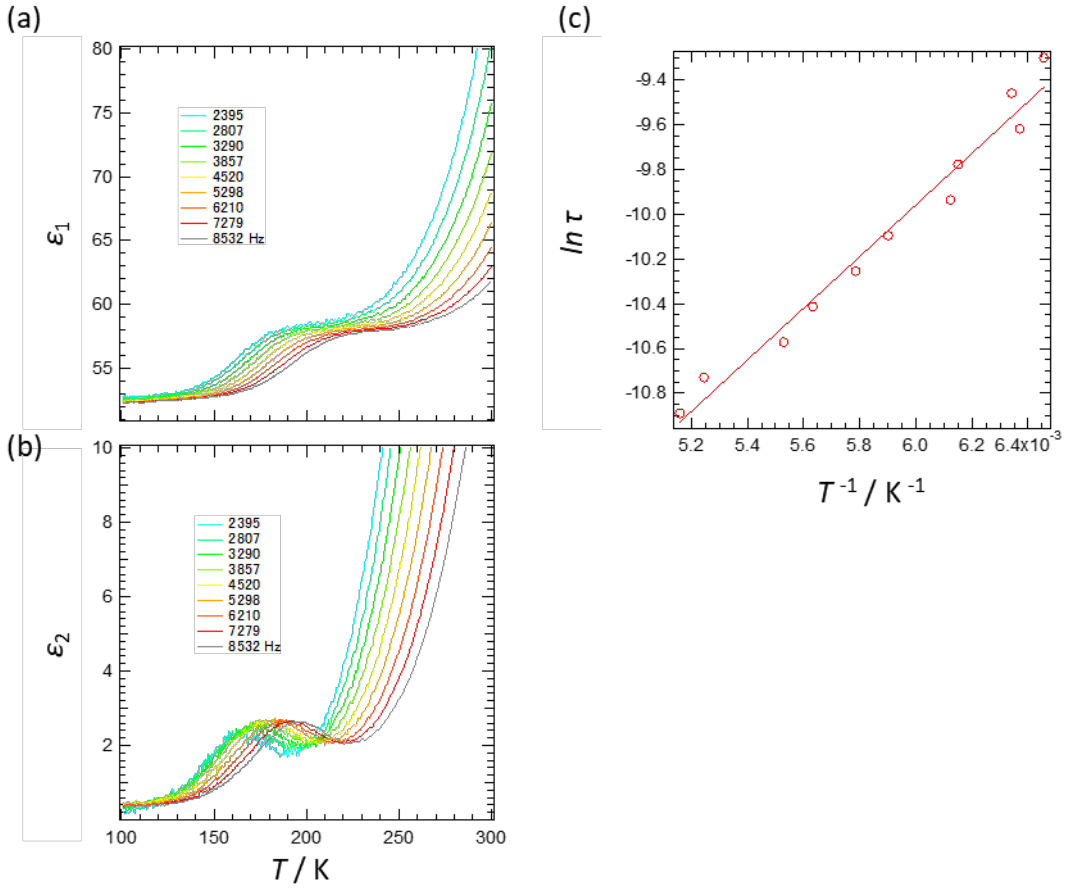

§Figure S4. (a) The real part and (b) imaginary part of the dielectric constant and (c) Arrhenius plot for dielectric relaxation.

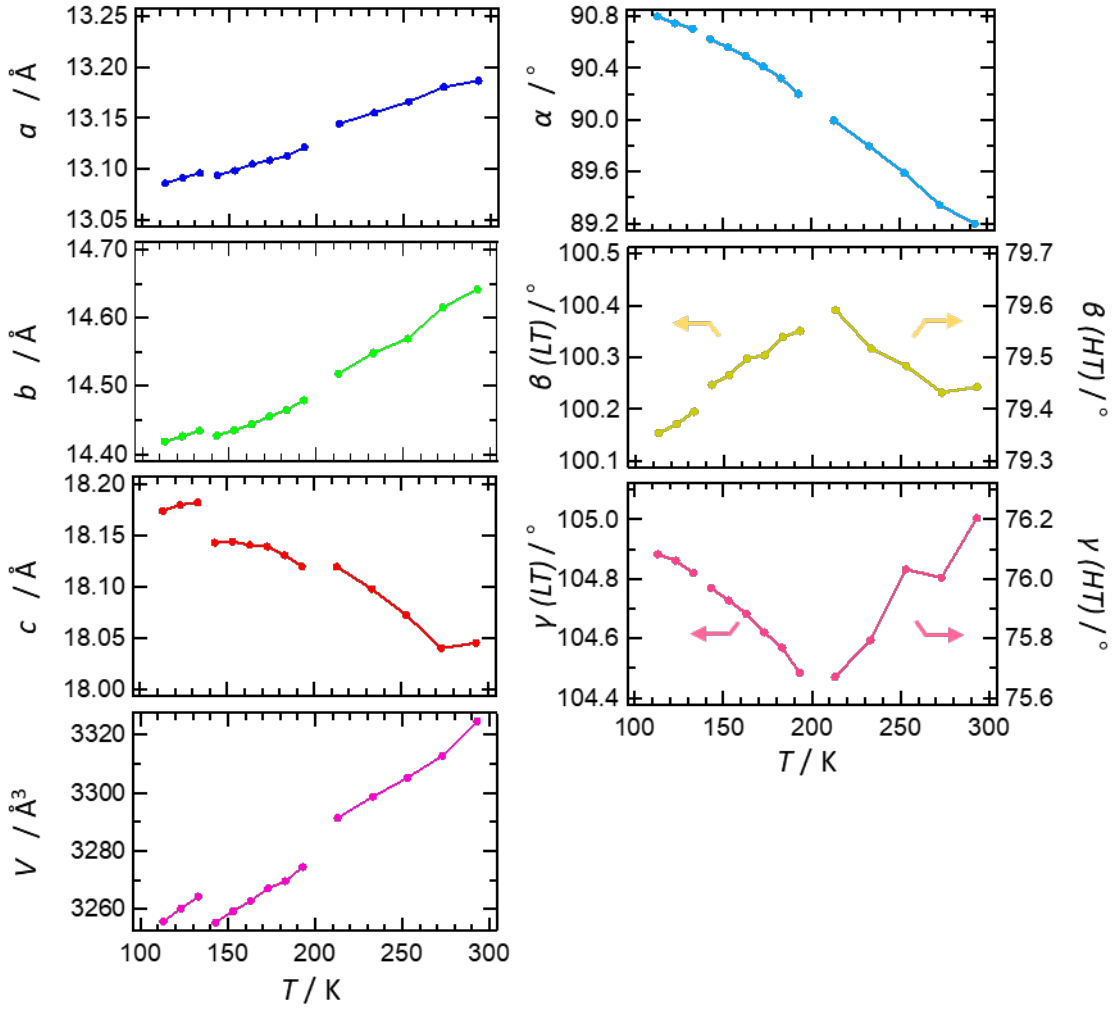

§Figure S5. Temperature dependence of unit cell dimensions and volume for crystal **1** over which the same crystal was studied. (HT : High Themperature phase, LT : Low Temperature phase)

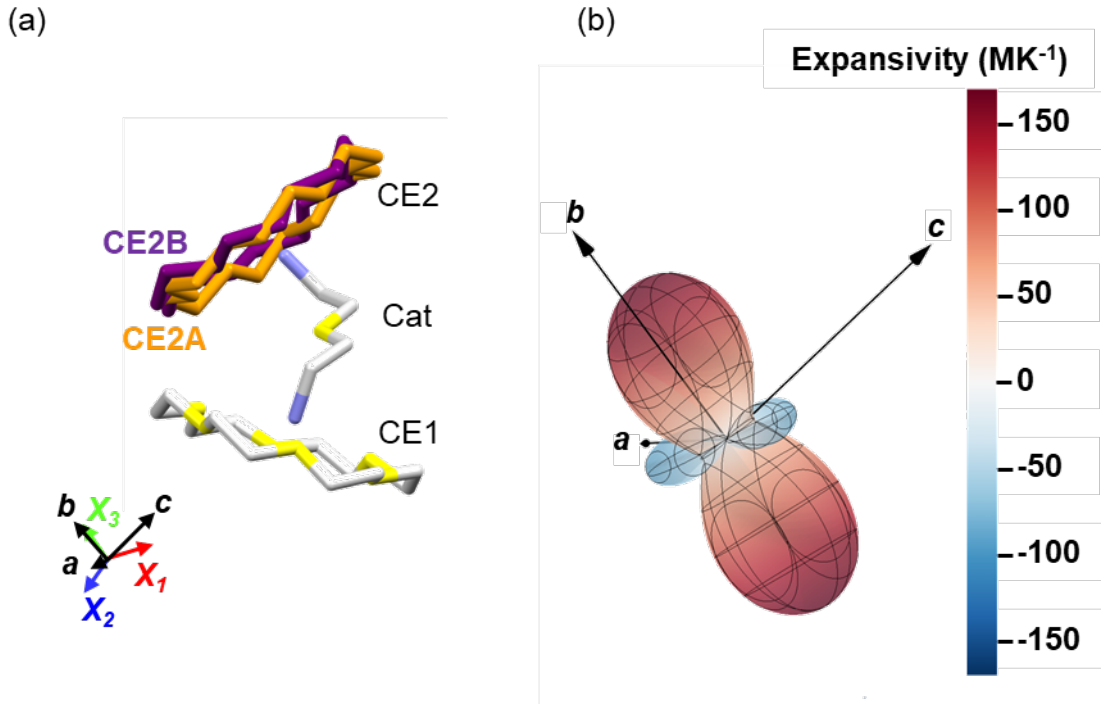

§Figure S6. The structure of supramolecular cations. Indicatrix plots for structural data of **1**. PASCal indicatrix Plotter was used to plot the data. The software was obtained from the web site: https://www.pascalapp.co.uk/

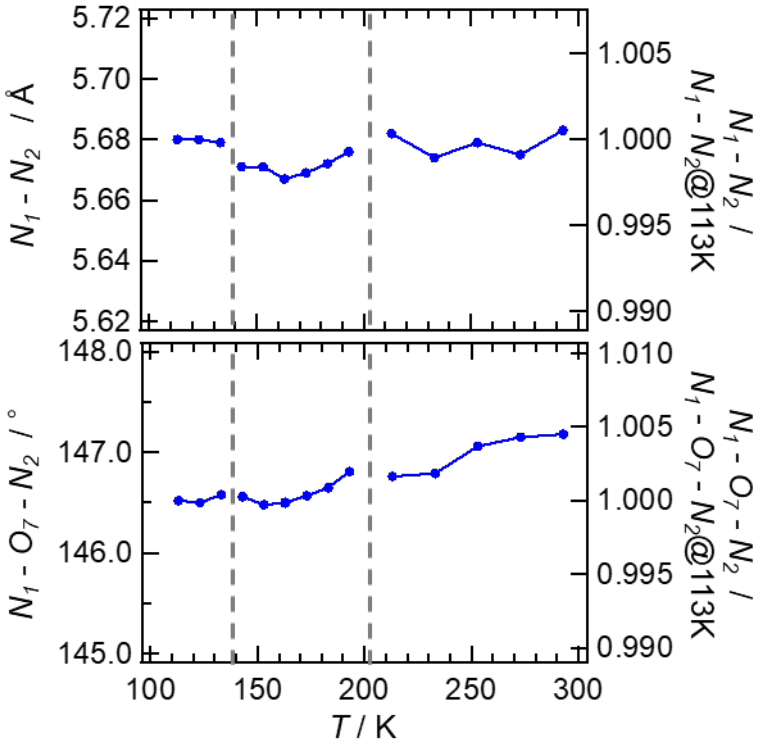

§Figure S7. Temperature dependence of the intramolecular N1•••N2 interatomic distance and N1•••O7•••N2 angles (left axis) and compared with each value at 113 K (right axis) for crystal **1**.

§Table S8. Crystal data, data collection, and reduction parameters for crystal **1**.

Crystal	**1**		
Temperature / K	113	123	133
Crystal Dimensions / mm³	0.1×0.5×0.7		
Chemical formula	$C_{40}H_{62}N_2Ni_2O_{13}S_{20}$		
Formula weight	1537.53		
Crystal system	*Triclinic*		
Space group	$P\bar{1}$		
a / Å	13.0860(3)	13.0913(3)	13.0962(3)
b / Å	14.4188(3)	14.4264(3)	14.4347(3)
c / Å	18.1738(4)	18.1799(4)	18.1822(5)
α / deg	90.798(2)	90.747(2)	90.702(2)
β / deg	100.154(2)	100.171(2)	100.195(2)
γ / deg	104.883(2)	104.861(2)	104.820(2)
V / Å^3	3255.84(13)	3260.32(13)	3264.37(14)
Z	2		
D_{calc} / g·cm^{-3}	1.568	1.566	1.564
μ(Mo K$_\alpha$) / cm^{-1}	1.274	1.272	1.271
$2\theta_{max}$ / *deg*	61.792	61.882	61.828
Reflections measured	43040	43134	43163
Independent reflections	16286	16308	16316
Reflections used	16286	16308	16316
R_1 [a]	0.0508	0.0523	0.0523
$R_w(F^2)$ [a]	0.1193	0.1223	0.1223
GOF	1.016	1.019	1.023
CCDC No.	2384649	2384650	2384651

[a] $R_1 = \Sigma||F_o| - |F_c|| / \Sigma|F_o|$ and $R_w = (\Sigma\omega(|F_o| - |F_c|)^2 / \Sigma\omega F_o^2)^{1/2}$.

Crystal	**1**		
Temperature / K	143	153	163
Crystal Dimensions / mm³	0.1×0.5×0.7		
Chemical formula	$C_{40}H_{62}N_2Ni_2O_{13}S_{20}$		
Formula weight	1537.53		
Crystal system	*Triclinic*		
Space group	$P\bar{1}$		
a / Å	13.0939(3)	13.0985(4)	13.1048 (4)
b / Å	14.4272(4)	14.4353(3)	14.4438(3)
c / Å	18.1428(4)	18.1439(5)	18.1407(5)
α / deg	90.624(2)	90.560(2)	90.492(2)
β / deg	100.247(2)	100.266(2)	100.298(2)
γ / deg	104.770(2)	104.728(2)	104.682(2)
V / Å^3	3255.51(13)	3259.35(15)	3262.86(15)
Z	2		
D_{calc} / g·cm^{-3}	1.568	1.567	1.565
μ(Mo K$_\alpha$) / cm^{-1}	1.274	1.273	1.271
$2\theta_{max}$ / *deg*	61.870	61.842	61.836
Reflections measured	43224	43335	43468
Independent reflections	16302	16329	16348
Reflections used	16302	16329	16348
R_1 [a]	0.0524	0.0532	0.0540
$R_w(F^2)$ [a]	0.1199	0.1232	0.1235
GOF	1.011	1.032	1.028
CCDC No.	2384652	2384653	2384654

[a] $R_1 = \Sigma||F_o| - |F_c|| / \Sigma|F_o|$ and $R_w = (\Sigma\omega(|F_o| - |F_c|)^2 / \Sigma\omega F_o^2)^{1/2}$.

Crystal	**1**		
Temperature / K	173	183	193
Crystal Dimensions / mm³	0.1×0.5×0.7		
Chemical formula	$C_{40}H_{62}N_2Ni_2O_{13}S_{20}$		
Formula weight	1537.53		
Crystal system	*Triclinic*		
Space group	$P\bar{1}$		
a / Å	13.1087(4)	13.1130(4)	13.1212 (4)
b / Å	14.4553(3)	14.4648(3)	14.4791(3)
c / Å	18.1391(5)	18.1307(5)	18.1199(5)
α / deg	90.412(2)	90.322(2)	90.200(2)
β / deg	100.304(2)	100.339(2)	100.351(2)
γ / deg	104.620(2)	104.569(2)	104.484(2)
V / Å^3	3267.30(15)	3269.70(15)	3274.58(15)
Z	2		
D_{calc} / g·cm^{-3}	1.563	1.562	1.559
μ(Mo K$_\alpha$) / cm^{-1}	1.270	1.269	1.267
$2\theta_{max}$ / *deg*	61.896	61.864	61.730
Reflections measured	43610	43704	43961
Independent reflections	16391	16409	16431
Reflections used	16391	16409	16431
R_1 [a]	0.0544	0.0551	0.0553
$R_w(F^2)$ [a]	0.1259	0.1263	0.1281
GOF	1.029	1.029	1.027
CCDC No.	2384655	2384656	2384657

[a] $R_1 = \Sigma||F_o| - |F_c|| / \Sigma|F_o|$ and $R_w = (\Sigma\omega(|F_o| - |F_c|)^2 / \Sigma\omega F_o^2)^{1/2}$.

Crystal	**1**		
Temperature / K	213	233	253
Crystal Dimensions / mm³	0.2×0.5×0.8		
Chemical formula	$C_{40}H_{62}N_2Ni_2O_{13}S_{20}$		
Formula weight	1537.53		
Crystal system	*Triclinic*		
Space group	$P\bar{1}$		
a / Å	13.1444(3)	13.1552(4)	13.1660(5)
b / Å	14.5178(5)	14.5482(6)	14.5697(6)
c / Å	18.1193(5)	18.0978(7)	18.0721(7)
α / deg	89.995(2)	89.797(3)	89.590(3)
β / deg	79.591(2)	79.517(3)	79.483(3)
γ / deg	75.671(2)	75.794(3)	76.032(3)
V / Å^3	3291.35(17)	3298.60(2)	3305.20(2)
Z	2		
D_{calc} / g·cm^{-3}	1.551	1.548	1.545
μ(Mo K$_\alpha$) / cm^{-1}	1.260	1.258	1.255
$2\theta_{max}$ / *deg*	52.746	52.744	52.744
Reflections measured	37421	38461	38905
Independent reflections	13452	13499	13529
Reflections used	13452	13499	13529
R_1 [a]	0.0551	0.0521	0.0514
$R_w(F^2)$ [a]	0.1367	0.1286	0.1276
GOF	1.037	1.044	1.034
CCDC No.	2384658	2384659	2384660

[a] $R_1 = \Sigma||F_o| - |F_c|| / \Sigma|F_o|$ and $R_w = (\Sigma\omega(|F_o| - |F_c|)^2 / \Sigma\omega F_o^2)^{1/2}$.

Crystal	**1**	
Temperature / K	273	293
Crystal Dimensions / mm³ /mm³	0.2×0.5×0.8	
Chemical formula	$C_{40}H_{62}N_2Ni_2O_{13}S_{20}$	
Formula weight	1537.53	
Crystal system	*Triclinic*	
Space group	$P\bar{1}$	
a / Å	13.1803(5)	13.1866(5)
b / Å	14.6150(7)	14.6416(5)
c / Å	18.0399(7)	18.0448(7)
α / deg	89.343(3)	89.198(3)
β / deg	79.432(3)	79.443(3)
γ / deg	76.004(4)	76.205(3)
V / Å³	3312.70(2)	3324.60(2)
Z	2	
D_{calc} / g·cm^{-3}	1.541	1.536
μ(Mo K$_\alpha$) / cm^{-1}	1.252	1.248
$2\theta_{max}$ / *deg*	52.738	52.744
Reflections measured	39008	39226
Independent reflections	13558	13618
Reflections used	13558	13618
R_1 [a]	0.0528	0.0516
$R_w(F^2)$ [a]	0.1338	0.1297
GOF	1.045	1.038
CCDC No.	2384661	2384662

[a] $R_1 = \Sigma||F_o| - |F_c|| / \Sigma|F_o|$ and $R_w = (\Sigma\omega(|F_o| - |F_c|)^2 / \Sigma\omega F_o^2)^{1/2}$.

§Table S9. output file of *PASCal* calculation for crystal **1** between 113 to 133 K.

Output			Direction		
Axes	α (M K^{-1})	σα (M K^{-1})	*a*	*b*	*c*
X_1	− 18.1210	1.8946	0.4630	− 0.600	0.6525
X_2	47.7425	0.2011	0.9470	0.1151	− 0.300
X_3	101.3108	0.5615	0.4420	0.7936	0.4181
V	130.9734	1.5332			

% Change in length						
T (K)	X_1 (%)	X_2 (%)	X_3 (%)	X_1,calc (%)	X_2,calc (%)	X_3,calc (%)
113	0	0	0	0.0027	0.0003	− 0.0008
123	− 0.0101	0.0486	0.0989	− 0.0154	0.048	0.1005
133	− 0.0362	0.0955	0.2026	− 0.0336	0.0958	0.2018

Volume		
T (K)	*V* (Å^3)	*V*lin (Å^3)
113	3255.843	3255.914
123	3260.319	3260.178
133	3264.372	3264.442

§Table S10. output file of *PASCal* calculation for crystal **1** between 143 to 193 K.

Output Axes	α (M K^{-1})	σ α (M K^{-1})	Direction *a*	*b*	*C*
X_1	− 74.1330	6.5341	0.4402	− 0.5167	0.7343
X_2	37.1844	0.6950	0.9111	− 0.1653	− 0.3776
X_3	152.3713	8.3966	0.5755	0.7713	0.2717
V	114.7932	2.6595			

% Change in length						
T / K	X_1	X_2	X_3	X_1, calc	X_2, calc	X_3, calc
143	0	0	0	0.0282	0.0035	− 0.0315
153	− 0.0413	0.0391	0.1201	− 0.0459	0.0407	0.1208
163	− 0.1050	0.0889	0.2418	− 0.1200	0.0779	0.2732
173	− 0.1597	0.1123	0.4101	− 0.1942	0.1150	0.4256
183	− 0.2595	0.1485	0.5483	− 0.2683	0.1522	0.5780
193	− 0.3771	0.1900	0.7761	− 0.3424	0.1894	0.7303

Volume		
T / K	*V* / Å^3	*V*lin / Å^3
143	3255.515	3255.541
153	3259.353	3259.278
163	3262.857	3263.016
173	3267.303	3266.753
183	3269.696	3270.490
193	3274.580	3274.227

§Table S11. output file of *PASCal* calculation for crystal **1** between 213 to 293 K.

Output			Direction		
Axes	α (M K^{-1})	σ α (M K^{-1})	*a*	*b*	*c*
X_1	− 104.9990	8.6499	− 0.3869	− 0.4653	0.7961
X_2	35.4035	2.6705	0.8997	0.2809	0.3342
X_3	193.7307	1.6950	− 0.6070	0.7617	0.2267
V	122.3889	7.3061			

% Change in length						
T / K	X_1	X_2	X_3	X_1, calc	X_2, calc	X_3, calc
213	0	0	0	− 0.0282	0.0013	− 0.0043
233	− 0.2243	0.0836	0.3619	− 0.2382	0.0721	0.3831
253	− 0.4879	0.1079	0.8051	− 0.4482	0.1430	0.7706
273	− 0.7329	0.2547	1.1353	− 0.6582	0.2138	1.1580
293	− 0.7957	0.2685	1.5506	− 0.8682	0.2846	1.5455

Volume		
T / K	*V* / Å^3	*V*lin / Å^3
213	3291.352	3290.371
233	3298.603	3298.427
253	3305.177	3306.484
273	3312.698	3314.540
293	3324.587	3322.597

§Reference

S1. G. Steimecke, H.-J. Sieler, R. Kirmse and E. Hoyer, *Phosphorus and Sulfur and the Related Elements*, 1979, **7**, 49–55.

S2. G. M. Sheldrick, *Acta Cryst A*, 2015, **71**, 3–8.

S3. O. V. Dolomanov, L. J. Bourhis, R. J. Gildea, J. a. K. Howard and H. Puschmann, *J Appl Cryst*, 2009, **42**, 339–341.

S4. M. J. Cliffe and A. L. Goodwin, *J Appl Cryst,* 2012, **45**, 1321–1329.

S5. G. A. Bain and J. F. Berry, *J. Chem. Educ.*, 2008, **85**, 532.

S6. T. Mori, A. Kobayashi, Y. Sasaki, H. Kobayashi, G. Saito and H. Inokuchi, *Bulletin of the Chemical Society of Japan*, 1984, **57**, 627–633.